Article type   : Research Article

Title

First Experimental Investigation of Simultaneously Tracking Two Independently Moving Targets on an MRI-Linac using Real-Time MRI and MLC Tracking

Running title

Multitarget tracking for an MRI-Linac

Authors

Paul Z. Y. Liu[1,2], Bing Dong[2], Doan Trang Nguyen[1,3], Yuanyuan Ge[1,4], Emily A. Hewson[1], David E. J. Waddington[1,2], Ricky O'Brien[1], Gary P. Liney[2,5,6,7], Paul J. Keall[1,2]

[1] ACRF Image X Institute, University of Sydney Central Clinical School, Sydney, NSW, Australia

[2] Department of Medical Physics, Ingham Institute for Applied Medical Research, Liverpool, NSW, Australia

[3] School of Biomedical Engineering, Faculty of Engineering and IT, University of Technology, Sydney, NSW, Australia

[4] Nelune Comprehensive Cancer Centre, Prince of Wales Hospital, Randwick, NSW, Australia

[5] Liverpool Cancer Therapy Centre, Radiation Physics, Liverpool, NSW, Australia

[6] School of Medicine, University of New South Wales, Sydney, NSW, Australia

[7] Centre for Medical Radiation Physics, University of Wollongong, Wollongong, NSW, Australia

Corresponding email: paul.liu@sydney.edu.au

Mailing address:

ACRF Image X Institute, Biomedical Building

1 Central Ave, Eveleigh, NSW, Australia 2015

Abstract

Purpose: High quality radiotherapy is challenging in cases where multiple targets with independent motion are simultaneously treated. A real-time tumor tracking system that can simultaneously account for the motion of two targets was developed and characterized.

Methods: The multitarget tracking system was implemented on an MRI-Linac and utilizes multi-leaf collimator (MLC) tracking to adapt the radiation beam to phantom targets reproducing motion with prostate and lung motion traces. Multitarget tracking consisted of three stages: (1) pre-treatment aperture segmentation where the treatment aperture was divided into segments corresponding to each target, (2) MR imaging where the positions of the two targets were localized and (3) MLC tracking where an updated treatment aperture was calculated. Electronic portal images (EPID) acquired during irradiation were analyzed to characterize geometric uncertainty and tracking latency.

Results: Multitarget MLC tracking effectively accounted for the motion of both targets during treatment. The root-mean square error between the centers of the targets and the centers of the corresponding MLC leaves were reduced from 5.5 mm without tracking to 2.7 mm with tracking for lung motion traces and reduced from 4.2 mm to 1.4 mm for prostate motion traces. The end-to-end latency of tracking was measured to be 328 ± 44 ms.

Conclusions: We have demonstrated the first experimental implementation of MLC tracking for multiple targets having independent motion. This technology takes advantage of the imaging capabilities of MRI-Linacs and would allow treatment margins to be reduced in cases where multiple targets are simultaneously treated.

Introduction

There are many cases of radiotherapy treatment that involve the simultaneous irradiation of multiple targets. For locally advanced non-small cell lung cancer, primary lung tumors are simultaneously treated with the mediastinal lymph nodes and up to 10% of patients will have multiple primary lung tumors.[1,2] For locally advanced prostate cancer, the prostate is simultaneously treated with the pelvic lymph nodes. Similarly, the treatment of oligometastatic cancers can include several small separate targets.

The accuracy and quality of treatment delivery in these cases can be compromised by the motion of the separate target volumes, which can be independent of one another. In non-small cell lung cancer, the relative movement between the primary lung tumor and the mediastinal lymph nodes can be greater than 10 mm[3,4], while in prostate cancer, the prostate can undergo up to 15 mm of motion during treatment relative to the pelvic lymph nodes.[5]

Despite the AAPM Task Group 76 recommendation for motion management if motion greater than 5 mm is observed, independent motion is not accounted for in current clinical practice.[6] As there is no ideal solution for multiple targets, the primary tumor is usually prioritized for interfraction or intrafraction motion. The margins of the secondary targets are expanded to not only account for their own motion, but also for the potential displacement of the primary target.[7] This method may lead to underdosing of the secondary target or the unnecessarily overdosing of surrounding healthy tissue. Independent target motion can be especially problematic for stereotactic body radiotherapy, which is becoming the preferred treatment modality for early stage primary or metastatic lung tumors but relies on tight margins and high geometric accuracy.[8,9]

One solution to improve treatment delivery of these challenging cases is to implement real-time image guidance and beam adaptation. This would allow margins to be reduced for one or both targets and allow dose to be escalated where necessary. While real-time image guidance technology for single targets has been implemented clinically[10,11], the extension of these solutions to multiple targets is not trivial for two reasons. (1) Accurate image-guidance is reliant on imaging to localize the position of the targets. Current solutions for single targets include on-board X-ray imaging, surface imaging and electromagnetic transponders. However, to the best of our knowledge, none of these technologies can localize multiple independently moving targets in real-time. (2) Many of the current approaches to real-time beam adaptation are unsuitable for multiple targets. There are currently four real-time beam adaptation techniques that have been implemented clinically for single targets: robotic, gimbaled, beam gating and multi-leaf collimator (MLC) tracking.[12] Of these, only MLC tracking has the capability to simultaneously account for the independent motion of multiple targets.

MRI-Linacs are a relatively new tool for radiotherapy and are an ideal platform for overcoming these two challenges. MRI-Linacs offer an unprecedented quality of real-time anatomical information including the motion of the target during treatment. As target volumes can be imaged directly in real-time using appropriately selected slices, multiple targets can be accurately localized during treatment. MLC tracking has been shown to be technically feasible on MRI-Linacs[13,14] and for tracking single targets, has been shown to have similar performance as MLC tracking on conventional linacs.[15,16]

In this work, we have developed a novel multitarget MLC tracking system for MRI-Linacs. A multitarget MLC tracking algorithm has been demonstrated on a conventional linear accelerator for a single target moving in combination with a second static target, as well as for target deformation[17]. This work extends this algorithm to simultaneously account for the motion of two targets. This work also describes the first implementation of multitarget tracking for an MRI-Linac environment, which leverages the superior imaging capabilities on this device.

Materials and Methods

Experimental setup

The MRI-Linac used for these experiments is a prototype system detailed in Liney *et al*.[18] The magnet (Agilent, UK) is a 1.0 T open bore design with a control system based on a Magnetom Avanto spectrometer (Siemens, Erlangen, Germany). The treatment beam is provided by a 6 MV linear accelerator (Linatron, Varex Imaging, UT, USA) with a 120-leaf (Millennium, Varian, Palo Alto, CA, USA) multileaf collimator (MLC). As shown in Figure 1, two MRI-visible spherical targets were set up inside the bore with Target 1 initially positioned at isocenter and Target 2 initially positioned 75 mm away in the anterior direction. Both targets were attached to a programmable MRI-compatible Quasar 1D motion phantom (Modus Medical Devices, Ontario, Canada). The motion phantom was modified to translate both targets in approximately equal and opposite directions along the superior-inferior (SI) axis.

The motion phantom was programmed with patient motion traces to analyze geometric accuracy and sinusoidal motion to analyze tracking latency. Three lung motion traces and three prostate motion traces were selected from a large database of CyberKnife Synchrony[19] and Calypso[5] (Varian) recorded motions, respectively. These were: a typical breathing trace (amplitude = 7 mm, period = 4 s), a high frequency breathing trace (amplitude = 6 mm, period = 2.5 s), a breathing trace with baseline drift (amplitude = 7 mm, period = 4 s, drift = 6 mm), a prostate trace with baseline drift (drift = 7 mm), a prostate trace with high frequency motion (motion range = 17 mm) and a prostate trace with erratic motion (motion range = 18

mm). These motion traces have been previously used in a multi-institutional study of real-time adaptive radiotherapy[20] and were selected to represent a variety of observed motion for lung and prostate tumors, two sites commonly treated with multiple targets.

As the motion phantom translated the two targets, they were irradiated with a single angle conformal treatment at a source-to-surface distance of 2.4 m. The multitarget tracking system updated the leaf positions of the MLC in real-time in order to maintain coverage of both targets. The multitarget tracking system consisted of three independent components: aperture segmentation, MR imaging and MLC tracking. These components are detailed below, and the overall workflow is shown in Figure 2.

Aperture segmentation (labelled 1 in figure 2)

Prior to treatment with multitarget MLC tracking, the original treatment plan was segmented using a multitarget algorithm previously described in Ge *et al*.[17] This algorithm separated the original MLC field (Figure 2A) into two segments corresponding to the two targets. The rectangle defined by the jaws in the beam's eye view (BEV) was first discretized to a 0.1 mm grid in the isocenter plane. The planning target volume (PTV) of each target at its original position was then projected onto the BEV and each grid element was assigned a value, represented as an image in Figure 2B with white representing no target, green representing Target 1 and red representing Target 2. The final values of the aperture grid were stored as a text file for access during treatment.

MR imaging (labelled 2 in figure 2)

During treatment, 2D cine-MR images were acquired to localize the position of each target. Sagittal slices were acquired using the true fast imaging with steady-state free precession (TRUFI) sequence. Images were acquired for a 200 mm square field of view and 10 mm slice thickness at a resolution of 64×64 pixels, resulting in a voxel size of $3.125 \times 3.125 \times 10$ mm. Geometric distortion of the MR images was not considered to require correction based on the data published by Shan et al[21]. The B0 inhomogeneity was optimized though active shimming and distortion caused by gradient non-linearity was minimal due to the small field of view and the limited range of the motion of the targets (maximum distance of 20 mm from isocenter). Imaging was performed using a 6/8 partial Fourier acquisition with TR = 3.54 ms and TE = 1.76 ms. The image acquisition time per frame was 171 ms with a 40 ± 5 ms gap between frames where magnet magnetization preparation occurs, resulting in a final image update rate of one frame every 211 ± 5 ms.

Using the Siemens Image Calculation Environment (ICE), the standard MR image reconstruction pipeline was modified to stream raw image frames from the MR Image Reconstruction computer immediately following reconstruction of *k*-space data within the ICE pipeline. Each frame of raw image data was

analyzed in real-time using in-house software to localize each target. The software used a template matching algorithm based on the OpenCV software library that calculated the normalized cross-correlation with half-pixel resolution (1.56 mm). The templates of the targets used for this process were delineated on an MR image acquired prior to irradiation (Figure 2C). For each cine-MR image, the position of each target was calculated (Figure 2D) and converted to a 2D vector that described the motion of that target from its original position in the BEV. The position vector was then transferred to the multitarget MLC tracking algorithm.

Multitarget MLC tracking (labelled 3 in figure 2)

With each updated position vector, the aperture grid was calculated pre-treatment was modified by translating the grid elements corresponding to each target by that target's motion (Figure 2F). An ideal MLC aperture was determined from the updated aperture grid by fitting the MLC leaves to the target shape. From the ideal MLC aperture, the closest matching deliverable MLC aperture was calculated using a direct optimization leaf sequencing algorithm that accounts for the physical limitations of the MLC such as finite leaf velocity, maximum travel range and adjacent leaf position (Figure 2E). This leaf sequencing algorithm has previously been implemented in single target MLC tracking for lung and prostate cancer patient treatmnts[10,22]. The updated leaf positions were sent to the MLC controller to achieve the final beam aperture that encompasses the motion of both targets.

Geometric accuracy

Images of the treatment beam acquired with an electronic portal imaging device (EPID) simultaneously captures both target motion and MLC adaptation and was independently used characterize geometric accuracy and system latency (Figure 2G). EPID images were acquired at 3.6 Hz and each frame was processed by subtracting a dark frame and applying a median filter to reduce noise introduced by the magnetic field of the MRI-Linac.

For each patient motion trace, the geometric accuracy was defined as the root mean square error (RMSE) between the position of the target centers, $P_{target}(t)$, of each target and center of that target's corresponding MLC leaf positions, $P_{MLC}(t)$, at time t. The centroid positions were automatically segmented using in-house software (Figure 2H) and the RMSE was calculated for three scenarios:

$$RMSE_{no\ tracking} = \sqrt{\frac{1}{T}\Sigma_{t=0}^{T}\left(P_{MLC}(0) - P_{target}(t)\right)^2} \qquad (1)$$

$$RMSE_{tracking} = \sqrt{\frac{1}{T}\Sigma_{t=0}^{T}\left(P_{MLC}(t) - P_{target}(t)\right)^2} \qquad (2)$$

$$RMSE_{latency\ corrected} = \sqrt{\frac{1}{T}\sum_{t=0}^{T}\left(P_{MLC}(t + \Delta T) - P_{target}(t)\right)^2} \qquad (3)$$

$RMSE_{no\ tracking}$ was the geometric uncertainty calculated for a treatment delivered with the original MLC aperture without MLC tracking. $RMSE_{tracking}$ was the geometric uncertainty calculated for a treatment delivered with multitarget MLC tracking. $RMSE_{latency\ corrected}$ was the geometric uncertainty when system latency was accounted in post-processing by shifting the phase of the MLC centroid positions by the tracking latency (ΔT). The calculation of $RMSE_{latency\ corrected}$ separates the geometric uncertainty arising from tracking latency from the geometric uncertainty arising from the other sources such as template matching and physical leaf motion.

Latency characterization

The end-to-end latency was defined as the time between when a moving target arrives at a particular position and when the center of the MLC leaves following that target arrives at the same position. To quantify the end-to-end latency, the motion phantom was programmed to move sinusoidally (amplitude = 20 mm, period = 7.5 and 10 s). As with the patient motion traces, the target and MLC centroids were automatically segmented from EPID images. A sinusoidal model with the equation:

$$P(t) = A\ sin(\ \omega(t + \varphi)\ ) \qquad (4)$$

was fitted to the centroid positions of the targets and apertures. The latency was calculated as the time difference between the two sinusoids averaged over both targets:

$$\Delta T = \varphi_{MLC} - \varphi_{target} \qquad (5)$$

Log files recorded during multitarget tracking were used to analyze the latency contributions of each step of the tracking workflow. The latency contributors were divided into three main sections: (1) MR imaging, defined as the time from when a target is imaged at a particular position P to when all data for that image has been transferred from the MRI, (2) target localization, defined as the time from when all image data was transferred to the time when a motion vector for position P was calculated and (3) MLC tracking, defined as the time from when the motion vector was received by the MLC tracking software to the time when the MLC leaves arrived at position P.

Template matching accuracy

The accuracy of the template matching algorithm in determining the location of the targets was analyzed by comparing the position calculated from MR images to the position reported by the analog output of the motion phantom. The analog output transmits a voltage signal directly from the electronic control box that

corresponds to the position of the motion phantom and was measured using an oscilloscope. The motion phantom was programmed to move sinusoidally (amplitude = 10 mm which was the maximum amplitude measurable by the oscilloscope, period = 7.5 s) and sinusoidal curves were fitted to the measured phantom positions. Once latency was accounted for, the accuracy of template matching was defined as the RMSE between the position reported by the motion phantom and the position calculated from MR images.

Results

Geometric accuracy

Figure 3 shows examples of the first 30 s of multitarget tracking for lung motion traces and the first 90 s of multitarget tracking for prostate motion traces. Figure 4 shows the difference between the target and aperture centroids and the RMSE for each motion trace. Overall, both targets are independently tracked with good agreement between the center of the target and that target's corresponding MLC aperture. The average RMSE was reduced from 5.5 mm without tracking to 2.7 mm with multitarget MLC tracking for lung motion traces and reduced from 4.2 mm to 1.4 mm for prostate motion traces.

As we will detail below, the system latency measured for the imaging parameters used was 328 ± 44 ms. The system latency is evident in Figure 3 with the aperture centroids trailing the target centroids. Accounting for the latency in post-processing, the RMSE was reduced to 1.2 mm for lung motion traces and 1.1 mm for prostate motion traces, shown in Figure 4. This showed that for the lung motion traces, this was the largest source of geometric uncertainty and RMSE was higher when tracking targets with higher frequency and magnitude of motion. For prostate motion traces where motion was slower, the geometric uncertainty was not heavily affected by latency. Contributions to geometric uncertainty other than latency include the uncertainty in template matching, uncertainty in target or aperture delineation in EPID images as well as inherent properties of the MLC such as the maximum leaf speed, control system update speed and leaf positioning errors.

The multitarget tracking algorithm tracks each target independently and in the same manner so the geometric uncertainty was expected to be the same for both targets. Across all six motion traces, the RMSE for Target 1 was 2.3 mm and the RMSE for Target 2 was 2.1 mm. The difference can be attributed to the smaller range of motion for Target 2 shown in Figure 5 and the higher signal to noise ratio of Target 2 in MR images shown in Figure 2D.

Latency characterization

Figure 5A shows the position of the target centroids and aperture centroids segmented from EPID images acquired during multitarget tracking of sinusoidal motion. The end-to-end latency was calculated to be 328 ± 44 ms when averaged over both targets and sinusoid periods of 7.5 and 10 s. Figure 5B shows the aperture centroids shifted by the measured latency.

Figure 6 shows the relative contributions of each of the sources of latency during each of the three stages of the tracking workflow. The linear encoding of k-space in the TRUFI sequence yields images where the target position corresponds to its location halfway through the MR acquisition when the central lines of k-space are acquired. The image update time (dark blue) was calculated as half of the total acquisition time for each image (half of 171 ms) plus the gap between frames (40 ± 5 ms). The reconstruction and data transfer time (light blue) was inferred by subtraction of all other components from the total latency.

Template matching accuracy

Figure 5C shows the position of Target 1 localized using template matching in cine-MR images compared to the position reported from the motion phantom's analog output. At an image resolution of 64 × 64 pixels, the RMSE was 0.51 mm. The accuracy of template matching is limited by the MR image resolution and after latency is the second largest source of geometric uncertainty. The accuracy of template matching can be improved with higher resolution MR images. For example, when the image size was increased to 128 × 128 pixels, the RMSE was reduced to 0.36 mm. However, the image update rate at this resolution decreases to one frame every 415 ± 8 ms, which in turn increases the system latency and negatively affects the overall efficacy of MLC tracking.

Discussion

In this work, we have developed and characterized a multitarget MLC tracking system on an MRI-Linac. We have shown that our end-to-end implementation was effective in accounting for motion of two targets moving with sinusoidal, lung and prostate motion traces.

The geometric uncertainty of was found to be similar to single target MLC tracking systems published in the literature. The latency corrected RMSE was 1.2 mm on average, which was comparable to the RMSE found on Varian (0.7 mm)[23] and Siemens (0.7 mm)[24] linear accelerators in studies that used prediction algorithms used to account for latency. The primary factors that affected the geometric uncertainty were system latency, imaging resolution and MLC performance.

The system latency (328 ± 44 ms) was found to be comparable to values published in the literature for single target MLC tracking systems based on kV images (550 ms imaging at 5 Hz)[25], electromagnetic transponders (230 ± 20 ms)[26] and with an Elekta Unity MRI-Linac (205 to 411 ms imaging at 4 to 8 Hz).[15]

The imaging capabilities of MRI-Linacs can greatly impact the safety and accuracy of radiotherapy, particularly at treatment sites with interfraction and intrafraction motion. Multitarget MLC tracking is a technology that takes full advantage of these imaging capabilities to enable real-time image guidance that would be too complex or not possible with standard linacs. Rather than attempting to cover the range of motion for both targets by expanding treatment margins, tracking each target independently would allow for treatment margins for each target to be kept as tight as possible whilst maintaining target coverage. Dose delivered to healthy tissue will be reduced and dose delivered to the target can be escalated if desired.

In order to further advance this technology and take it from phantom experiments to patient treatments, several improvements could be made to overcome some of the experimental limitations and improve the robustness of the technology. These are discussed below.

(1) While the multitarget tracking algorithm accounts for motion in 3D, currently only 1D MRI-compatible motion phantoms are commercially available which limited the complexity of patient motion that could be achieved. In the case of 3D motion, the targets are translated in the updated aperture grid (Figure 2F) for motion in the plane of the BEV and magnified or shrunk for motion along the beam axis[27,28]. Target motion that is perpendicular to the MLC leaves or along the beam axis can compromise an exact leaf fitting to the target shape and has been shown to affect tracking accuracy in single target MLC tracking[25]. Ideally, a 6 degree-of-freedom MRI-compatible motion phantom[29] would be available to assess tracking performance with 3D target motion. Furthermore, two separate motion phantoms with an independent input motion trace for each target would bring these phantom experiments closer to replicating patient motion.

(2) A conformal treatment at a single gantry angle was used for this work. The implementation of multitarget MLC tracking with IMRT or VMAT will increase its complexity, though its feasibility has been demonstrated on conventional linacs by Ge *et al.*[17] IMRT and VMAT treatments require separate aperture grids (Figure 2B) to be generated for each control point or gantry angle prior to treatment. During irradiation, the control point or gantry angle is monitored as the treatment progresses and corresponding aperture grids are accessed for tracking. The geometry of IMRT and VMAT treatments may also introduce situations where the two targets overlap in the BEV. In these situations, the aperture grids would record the overlapping areas within the grid elements and the MLC leaves are fitted to a union of the two target shapes. While the resultant MLC aperture maintains coverage of both targets, the merging of different parts

of the aperture could alter the total irradiated area for a given control point and cause the dose delivered to the targets or nearby organs to differ from the planned dose. In many cases, beam angles where the targets overlap could be avoided during treatment planning or a temporary beam gate could be triggered when overlap is detected during imaging, however further investigation is required to fully understand the effects of overlapping targets.

(3) Both targets were translated in the same MR imaging slice, that is, both targets were at the same depth along the beam central axis. In a clinical scenario, it is likely that each target would be in a separate imaging plane and cannot be tracked by imaging a single 2D slice. One solution would be to acquire multiple MR slices, however, performing multi-slice imaging with a single-channel MR body coil as the receive coil would require slices to be acquired in an alternating manner. This would increase latency and geometric uncertainty.[30] The implementation of multi-channel receive arrays will enable the use of parallel imaging and simultaneous multi-slice techniques that significantly improve imaging speed and volume coverage.[31,32]

(4) The MR imaging parameters and template matching algorithm worked well for spherical phantoms in air but have not been optimized for patients. The 64×64 pixel image size was selected to reduce tracking latency and may be of inadequate spatial resolution for real anatomy. The template matching algorithm was accurate but does not account for target rotation, scaling or deformation that would occur with patient imaging. Furthermore, patient images would require a larger field of view to avoid folding artifacts, increasing voxel size and reduce spatial resolution during tracking. A larger field of view may also introduce significant geometric distortion for off-axis targets due to gradient non-linearity. Distortion correction algorithms based on spherical harmonics and the inverse electromagnetic method would need to be applied to maintain geometric accuracy during tracking.[21]

While solutions to these four challenges exist in the literature, the risk in their implementation for multitarget tracking is that they may increase the end-to-end latency. Latency is critical to the performance of MLC tracking not only because it is the primary source of geometric uncertainty, but also because it determines the effectiveness of the prediction algorithms that are used to compensate for it. The accuracy of prediction algorithms have been shown to diminish with longer prediction horizons.[33,34] While the current measured latency of 328 ± 44 ms is within the latency period that can be accurately predicted,[35,36] the implementation of the additional steps and algorithms could increase the latency beyond the point at which prediction algorithms are effective.

Figure 6 shows that computational contributions to the total end-to-end latency, for example template matching or leaf optimization, are small compared to the contributions of MR imaging (in blue) and physical leaf motion (in light red). As the latency of physical leaf motion is an inherent property of the hardware, improvements in MRI acquisition and reconstruction can result in the greatest reduction in system latency. Novel MR imaging techniques such as golden angle radial imaging and machine learning based image reconstruction can localize targets via under-sampled *k*-space data, reducing the total imaging time, decreasing system latency and improving the efficacy of motion prediction algorithms.[37]

Conclusion

For radiotherapy treatments with multiple targets, for example a primary tumor treated with nearby nodes or treatment of oligometastases, independent motion of the targets can compromise treatment delivery. We have developed a multitarget tumor tracking system for an MRI-Linac that can adapt a treatment beam in real-time to compensate for motion of multiple targets. The clinical realization of this technology would allow target margins to be reduced, minimizing healthy tissue toxicity whilst maintaining coverage of multiple targets.

Acknowledgements

Conflict of Interest

PJK is an inventor on US patents 7,469,035 and 8,971,489 that are related to MLC tracking. Patent 7,469,035 is unlicensed; patent 8,971,489 is exclusively licensed to Asto CT.

References

1. Creach KM, Bradley JD, Mahasittiwat P, Robinson CG. Stereotactic body radiation therapy in the treatment of multiple primary lung cancers *Radiother Oncol.* 2012;104(1):19-22.
2. Tsunezuka Y, Matsumoto I, Tamura M, et al. The results of therapy for bilateral multiple primary lung cancers: 30 years experience in a single centre *Eur J Surg Oncol.* 2004;30(7):781-785.

3. Pantarotto JR, Piet AH, Vincent A, van Sornsen de Koste JR, Senan S. Motion analysis of 100 mediastinal lymph nodes: potential pitfalls in treatment planning and adaptive strategies *Int J Radiat Oncol Biol Phys.* 2009;74(4):1092-1099.

4. Schmidt ML, Hoffmann L, Knap MM, et al. Cardiac and respiration induced motion of mediastinal lymph node targets in lung cancer patients throughout the radiotherapy treatment course *Radiother Oncol.* 2016;121(1):52-58.

5. Langen KM, Willoughby TR, Meeks SL, et al. Observations on real-time prostate gland motion using electromagnetic tracking *International Journal of Radiation Oncology Biology Physics.* 2008;71(4):1084-1090.

6. Keall PJ, Mageras GS, Balter JM, et al. The management of respiratory motion in radiation oncology report of AAPM Task Group 76 *Med Phys.* 2006;33(10):3874-3900.

7. Xia T, Li H, Sun Q, et al. Promising clinical outcome of stereotactic body radiation therapy for patients with inoperable Stage I/II non-small-cell lung cancer *Int J Radiat Oncol Biol Phys.* 2006;66(1):117-125.

8. Ball D, Mai GT, Vinod S, et al. Stereotactic ablative radiotherapy versus standard radiotherapy in stage 1 non-small-cell lung cancer (TROG 09.02 CHISEL): a phase 3, open-label, randomised controlled trial *Lancet Oncol.* 2019;20(4):494-503.

9. Li Q, Mu J, Gu W, et al. Frameless stereotactic body radiation therapy for multiple lung metastases *J Appl Clin Med Phys.* 2014;15(4):4737.

10. Booth JT, Caillet V, Hardcastle N, et al. The first patient treatment of electromagnetic-guided real time adaptive radiotherapy using MLC tracking for lung SABR *Radiother Oncol.* 2016;121(1):19-25.

11. Mittauer K, Paliwal B, Hill P, et al. A New Era of Image Guidance with Magnetic Resonance-guided Radiation Therapy for Abdominal and Thoracic Malignancies *Cureus.* 2018;10(4):e2422.

12. Bertholet J, Knopf A, Eiben B, et al. Real-time intrafraction motion monitoring in external beam radiotherapy *Phys Med Biol.* 2019;64(15):15TR01.

13. Yun J, Wachowicz K, Mackenzie M, Rathee S, Robinson D, Fallone BG. First demonstration of intrafractional tumor-tracked irradiation using 2D phantom MR images on a prototype linac-MR *Med Phys.* 2013;40(5):051718.

14. Crijns SP, Raaymakers BW, Lagendijk JJ. Proof of concept of MRI-guided tracked radiation delivery: tracking one-dimensional motion *Phys Med Biol.* 2012;57(23):7863-7872.

15. Glitzner M, Woodhead PL, Borman PTS, Lagendijk JJW, Raaymakers BW. Technical note: MLC-tracking performance on the Elekta unity MRI-linac *Phys Med Biol.* 2019;64(15):15NT02.

16. Menten MJ, Fast MF, Nill S, Kamerling CP, McDonald F, Oelfke U. Lung stereotactic body radiotherapy with an MR-linac - Quantifying the impact of the magnetic field and real-time tumor tracking *Radiother Oncol.* 2016;119(3):461-466.

17. Ge Y, O'Brien RT, Shieh CC, Booth JT, Keall PJ. Toward the development of intrafraction tumor deformation tracking using a dynamic multi-leaf collimator *Med Phys.* 2014;41(6):061703.

18. Liney GP, Dong B, Weber E, et al. Imaging performance of a dedicated radiation transparent RF coil on a 1.0 Tesla inline MRI-linac *Phys Med Biol.* 2018;63(13):135005.

19. Suh Y, Dieterich S, Cho B, Keall PJ. An analysis of thoracic and abdominal tumour motion for stereotactic body radiotherapy patients *Phys Med Biol.* 2008;53(13):3623-3640.

20. Colvill E, Booth J, Nill S, et al. A dosimetric comparison of real-time adaptive and non-adaptive radiotherapy: A multi-institutional study encompassing robotic, gimbaled, multileaf collimator and couch tracking *Radiother Oncol.* 2016;119(1):159-165.

21. Shan S, Liney GP, Tang F, et al. Geometric distortion characterization and correction for the 1.0 T Australian MRI-linac system using an inverse electromagnetic method *Med Phys.* 2020;47(3):1126-1138.

22. Colvill E, Booth JT, O'Brien RT, et al. Multileaf Collimator Tracking Improves Dose Delivery for Prostate Cancer Radiation Therapy: Results of the First Clinical Trial *Int J Radiat Oncol Biol Phys.* 2015;92(5):1141-1147.

23. Ravkilde T, Keall PJ, Hojbjerre K, Fledelius W, Worm E, Poulsen PR. Geometric accuracy of dynamic MLC tracking with an implantable wired electromagnetic transponder *Acta Oncol.* 2011;50(6):944-951.

24. Krauss A, Nill S, Tacke M, Oelfke U. Electromagnetic real-time tumor position monitoring and dynamic multileaf collimator tracking using a Siemens 160 MLC: geometric and dosimetric accuracy of an integrated system *Int J Radiat Oncol Biol Phys.* 2011;79(2):579-587.

25. Poulsen PR, Cho B, Ruan D, Sawant A, Keall PJ. Dynamic multileaf collimator tracking of respiratory target motion based on a single kilovoltage imager during arc radiotherapy *Int J Radiat Oncol Biol Phys.* 2010;77(2):600-607.

26. Keall PJ, Colvill E, O'Brien R, et al. The first clinical implementation of electromagnetic transponder-guided MLC tracking *Med Phys.* 2014;41(2):020702.

27. Sawant A, Venkat R, Srivastava V, et al. Management of three-dimensional intrafraction motion through real-time DMLC tracking *Med Phys.* 2008;35(5):2050-2061.

28. Toftegaard J, Keall PJ, O'Brien R, et al. Potential improvements of lung and prostate MLC tracking investigated by treatment simulations *Med Phys.* 2018;45(5):2218-2229.

29. Krieger A, Iordachita, II, Guion P, et al. An MRI-compatible robotic system with hybrid tracking for MRI-guided prostate intervention *IEEE Trans Biomed Eng.* 2011;58(11):3049-3060.

30. Poulsen PR, Knap MM, Brix L, Sørensen TS, Schmidt ML, Pedersen EM. Real-Time Magnetic Resonance Imaging of Simultaneous Lung Tumor Motion and Involved Mediastinal Lymph Node Motion *International Journal of Radiation Oncology Biology Physics.* 2016;96(2):E686-E687.

31. Barth M, Breuer F, Koopmans PJ, Norris DG, Poser BA. Simultaneous multislice (SMS) imaging techniques *Magn Reson Med.* 2016;75(1):63-81.

32. Zijlema SE, Tijssen RHN, Malkov VN, et al. Design and feasibility of a flexible, on-body, high impedance coil receive array for a 1.5 T MR-linac *Phys Med Biol.* 2019;64(18):185004.

33. Ernst F, Durichen R, Schlaefer A, Schweikard A. Evaluating and comparing algorithms for respiratory motion prediction *Phys Med Biol.* 2013;58(11):3911-3929.

34. Sharp GC, Jiang SB, Shimizu S, Shirato H. Prediction of respiratory tumour motion for real-time image-guided radiotherapy *Phys Med Biol.* 2004;49(3):425-440.

35. Johl A, Ehrbar S, Guckenberger M, et al. Performance comparison of prediction filters for respiratory motion tracking in radiotherapy *Med Phys.* 2020;47(2):643-650.

36. Krauss A, Nill S, Oelfke U. The comparative performance of four respiratory motion predictors for real-time tumour tracking *Phys Med Biol.* 2011;56(16):5303-5317.

37. Borman PTS, Tijssen RHN, Bos C, Moonen CTW, Raaymakers BW, Glitzner M. Characterization of imaging latency for real-time MRI-guided radiotherapy *Phys Med Biol.* 2018;63(15):155023.
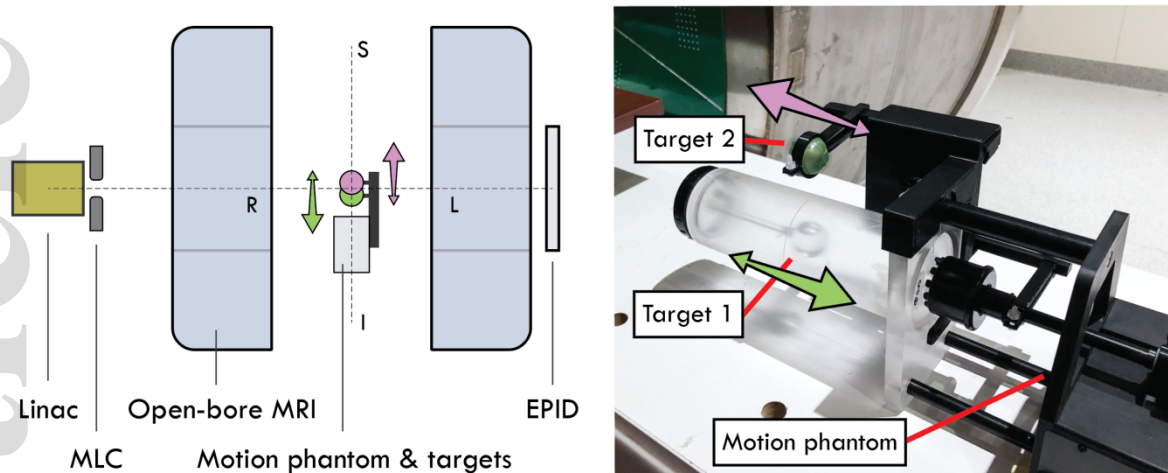
Figure 1. (Left) Schematic of the multitarget MLC tracking experimental set up. Target motion and MR imaging occur in the superior-inferior (SI) plane, while the main magnetic field is parallel to the left-right (LR) axis. (Right) Photo showing the 1D motion phantom modified to simultaneously translate both targets in opposite directions. A video of the motion phantom can be found in the supplementary material.
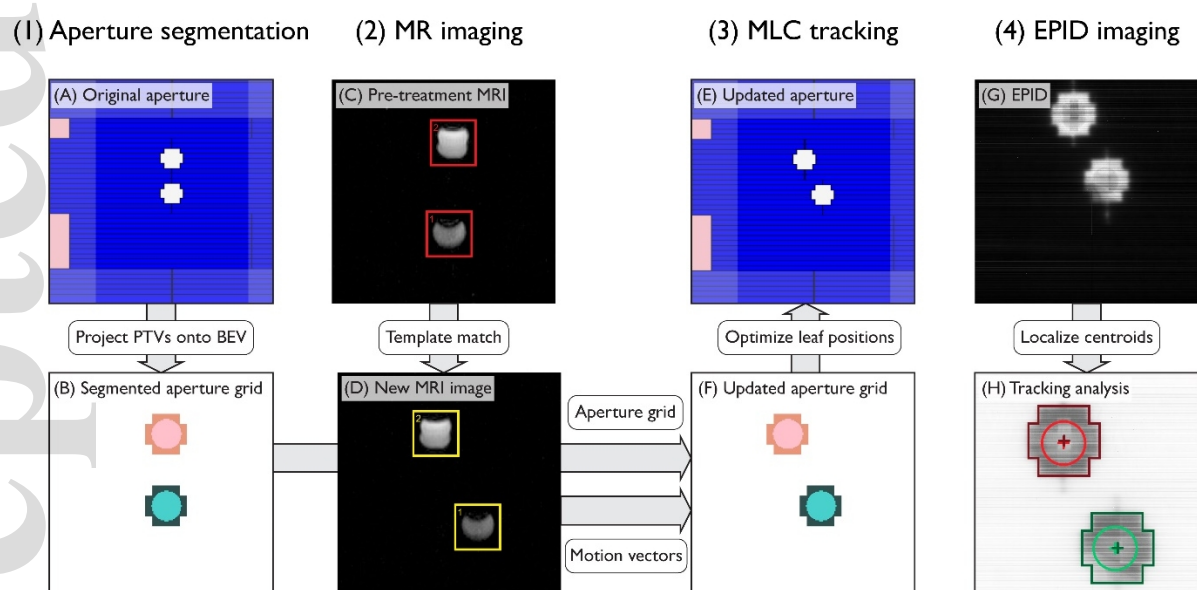

Figure 2. End-to-end workflow for multitarget MLC tracking and EPID analysis. Steps A to C are performed pre-treatment, steps D to G are performed during treatment and step H is performed post-treatment. Videos of MR imaging (step D), the updated MLC apertures (step E) and EPID imaging (step H) during multitarget MLC tracking can be found in the supplementary material.
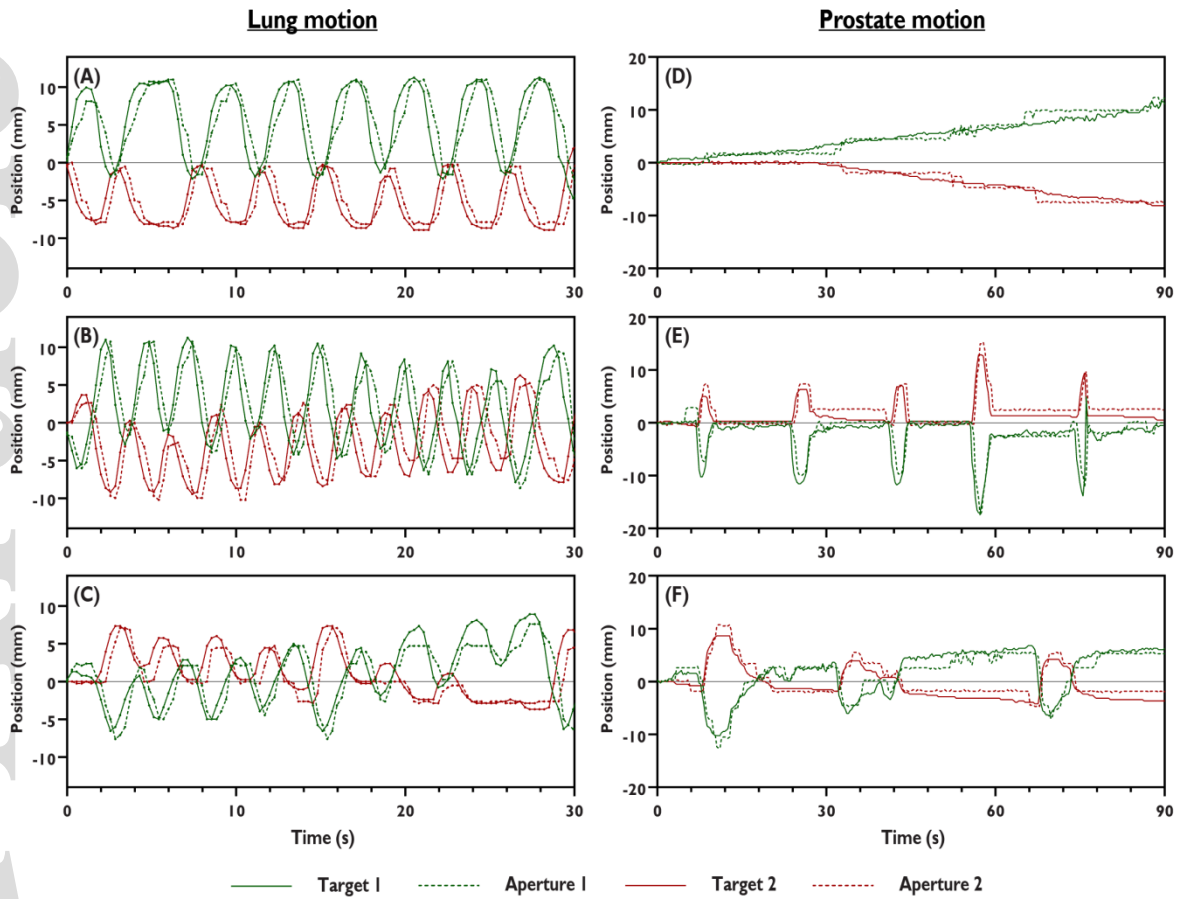
Lung motion   **Prostate motion**

——— Target 1   ·········· Aperture 1   ——— Target 2   ·········· Aperture 2

Figure 3. Examples of multitarget tracking for (A) typical lung motion, (B) high frequency lung motion, (C) lung motion with baseline drift, (D) prostate motion with baseline drift, (E) high frequency prostate motion and (F) erratic prostate motion. The solid lines represent the centroids of each target and the dotted lines represent the centers of each target's corresponding apertures, both delineated from EPID images.
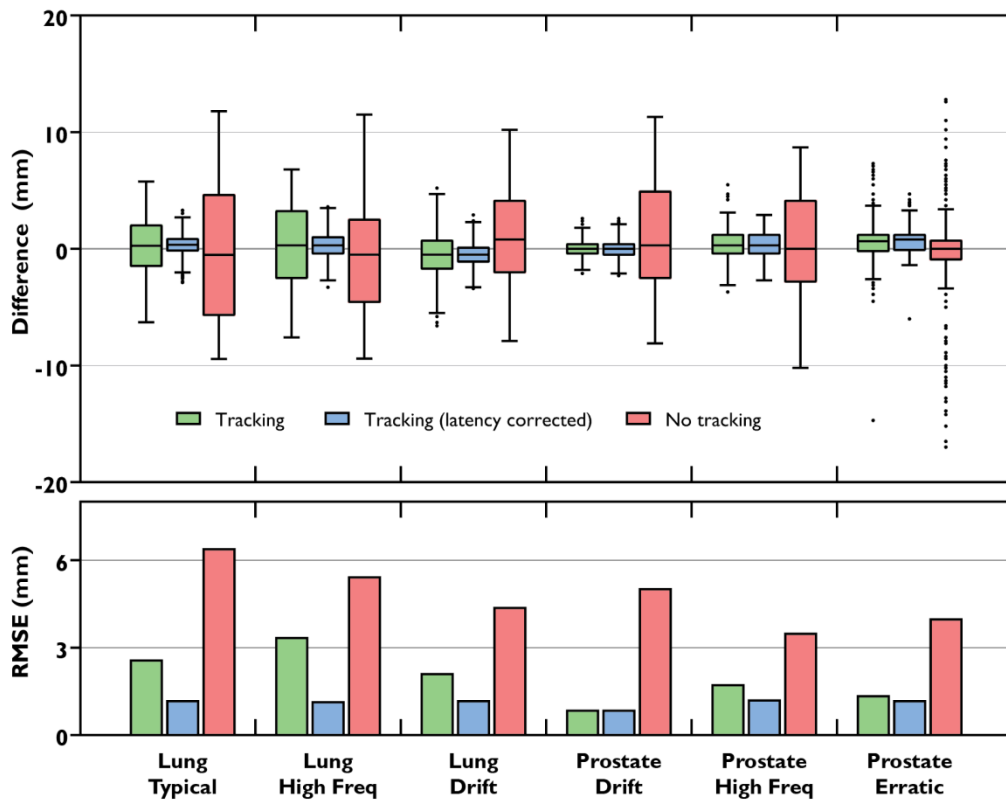
Figure 4. The difference between the target centroids and aperture centroids (top) and the RMSE (bottom) for the six motion traces. Tracking (green) represents the geometric error for both targets tracked with multitarget MLC tracking. Latency corrected (blue) represents the geometric error with the aperture positions shifted by the measured system latency ΔT (328 ms). No tracking (red) represents the geometric error when the apertures are in their original positions.
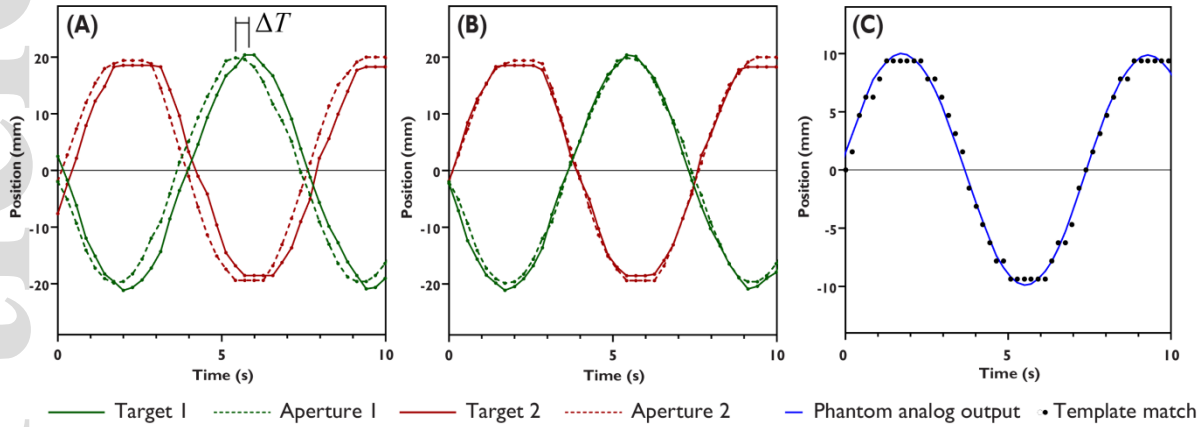
Figure 5. (A) Example of multitarget tracking for sinusoidal motion. Sinusoids fitted to the data were used to calculate the system latency (ΔT). The solid lines represent the centroids of each target and the dotted lines represent the centers of each target's corresponding apertures, both delineated from EPID images. (B) The aperture centroids shifted by ΔT show good agreement with target centroids. (C) The position of Target 1 calculated from 64×64 pixel cine-MR images compared to the raw position output of the motion phantom.
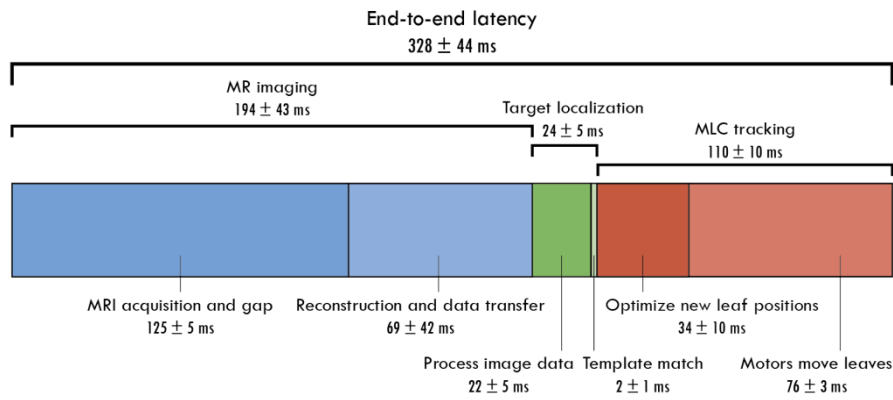

Figure 6. The components sources of latency during each stage of the multitarget MLC tracking workflow.